Journal of Alloys and Compounds 1068 (2026) 188535

Contents lists available at ScienceDirect

Journal of Alloys and Compounds

journal homepage: www.elsevier.com/locate/jalcom

High-frequency soft magnetic performance of Fe-based nanocrystalline alloys through stepwise transverse magnetic field annealing

Jifeng Zhou[1], Chi Ren[1], Qianqian Liu, Jun Li, Fan Hu, Qianqian Wang, Xingdu Fan, Zhe Jia, Qiang Luo*, Zhijun Guo*, Baolong Shen

School of Materials Science and Engineering, Jiangsu Key Laboratory for Advanced Metallic Materials, Southeast University, Nanjing 211189, China

ARTICLE INFO

Keywords:
Fe-based nanocrystalline alloy
Transverse magnetic field annealing
Magnetic anisotropy control
Domain structure evolution
High-frequency permeability stability

ABSTRACT

High-frequency soft magnetic applications impose strict requirements on permeability stability, core loss, and coercivity in Fe-based nanocrystalline alloys. In this study, $Fe_{69.5}Co_3Nb_2Mo_{1.5}Si_{14}B_9Cu_1$ alloys were processed using a stepwise transverse magnetic field annealing route consisting of conventional nanocrystallization followed by low-temperature transverse-field treatment. The stepwise process enables independent control of nanocrystalline structure and magnetic anisotropy, preserving a refined grain size of ~12 nm while significantly enhancing the crystalline volume fraction. Compared with conventional annealing and single-step transverse magnetic field annealing, the optimized alloy exhibits an effective permeability of about 46,000 at 1 kHz and 29,300 at 100 kHz, together with low coercivity (0.45 A/m) and reduced core loss (398 kW/m^3 at 100 kHz and 0.2 T). Magnetic domain observations indicate that the improved performance is associated with optimized anisotropy and a mixed magnetization process involving domain-wall motion and rotation. The results demonstrate the effectiveness of stepwise anisotropy regulation for improving the high-frequency soft magnetic properties of Fe-based nanocrystalline alloys.

1. Introduction

The rapid deployment of third-generation wide bandgap (WBG) semiconductors is driving modern power-electronic systems toward higher switching frequencies, increased power density, miniaturization, and improved energy efficiency [1,2]. In high-frequency power conversion systems, WBG semiconductors are typically integrated with soft magnetic materials that play essential roles in energy storage and electromagnetic regulation [3–5]. Their performance is governed primarily by magnetic permeability, which reflects the responsiveness of soft magnetic materials to external magnetic fields [6] and directly influences the sensitivity of electronic devices [7]. Consequently, applications operating in the medium-to-high frequency range (1–100 kHz) impose strict requirements on soft magnetic materials. Therefore, it is a critical demand for materials that exhibit both high permeability and superior frequency stability.

Fe-based nanocrystalline alloys have emerged as leading candidates due to their excellent comprehensive soft magnetic properties [8]. Nevertheless, except for nanocrystalline ultrathin ribbons geometries (below 16 μm), the permeability of Fe-based nanocrystalline alloys at 100 kHz typically below 25,000, falling short of the stringent application requirements of WBG devices under high-frequency [28]. More broadly, the rapid degradation of permeability with increasing frequency remains a pervasive limitation across most soft magnetic materials, posing a fundamental challenge for high-frequency operation. Strategies such as micro-alloying [6,9–11] and ribbons thinning [12] have delivered partial improvements, yet they often involve unavoidable trade-offs among effective permeability (μ_e), core loss (P_{cv}) and coercivity (H_c) under high frequency conditions [13]. In the pursuit of higher saturation magnetic flux density (B_s), it is essential to reduce high-frequency P_{cv} and mitigate the rapid decay of μ_e, as these factors constitute bottlenecks in the development of soft magnetic materials [14–16]. Achieving a synergistic balance among these parameters at elevated frequencies therefore remains an unresolved challenge [17].

Magnetic anisotropy engineering offers an effective pathway to overcoming this limitation [18]. Field-induced magnetic anisotropy (K_u), engineered through magnetic field annealing, is pivotal in regulating the hysteresis behavior and governing magnetization dynamics in

---

* Corresponding authors.
E-mail addresses: q.luo@seu.edu.cn (Q. Luo), zj-guo@seu.edu.cn (Z. Guo).

[1] These authors contribute equally to this work as co-first authors.

https://doi.org/10.1016/j.jallcom.2026.188535
Received 5 February 2026; Received in revised form 6 April 2026; Accepted 8 May 2026

nanocrystalline alloys. According to previous study, longitudinal magnetic field annealing (LFA) imparts a significant longitudinal magnetic anisotropy ($K_u \approx 404$–867 J/m^3) to $Fe_{75}Co_8(B_{10}Si_3C_3P_1)_{1-x/17}Cu_x$ alloys. This anisotropy serves as a driving force for the alignment of regular longitudinal domains, which in turn significantly enhances magnetic softness, evidenced by a minimum coercivity of 1.6 A/m [19]. Wang et al. reported that rotating magnetic field annealing (RFA) significantly suppresses the K_u of $(Fe_{0.9}Co_{0.1})_{73.5}Cu_1Nb_3Si_{13.5}B_9$ alloy with a minimum of 72 J/m^3 [20]. This suppression effectively inhibits the establishment of a uniaxial easy axis, thereby facilitating the averaging of local magnetocrystalline anisotropy, which facilitated the averaging of local magneto-crystalline anisotropy and produced an optimized soft magnetic performance with simultaneously improved B_s (1.42 T) and ultra-low H_c (1.5 A/m). Specifically, transverse field annealing (TFA) has proven particularly effective for directional control of K_u in high-frequency applications. Madugundo et al. reported that TFA applied to $Fe_{74.1}Si_{15.7}Nb_{3.1}B_{6.1}Cu_1$ produced a flattened *B-H* loop with a K_u of 41 J/m^3 and a markedly increased cut-off frequency [21]. To enable finer regulation of K_u, Herzer subsequently proposed a stepwise transverse magnetic field annealing strategy, consisting of high-temperature nanocrystallization without a magnetic field followed by low-temperature transverse-field annealing (573–813 K) [22,23]. In contrast to direct high-temperature field annealing—which induces a saturated, maximum K_u insensitive to processing time—this stepwise route allows K_u to be effectively reduced and continuously tuned. Crucially, this method allows for the effective reduction and tuning of K_u, which directly dictates the underlying magnetization mechanism. Flohrer et al. demonstrated that strong K_u favors coherent magnetization rotation, whereas a controlled weak K_u (achieved via stepwise annealing) shifts the mechanism toward inhomogeneous rotation and domain nucleation [24–26]. Such domain refinement is particularly beneficial for suppressing dynamic residual losses at elevated frequencies. Despite these advances, establishing a clear and quantitative correlation among stepwise annealing parameters, the precise magnitude of induced K_u, and the associated evolution of magnetic domain structures remains challenging.

Previous studies have established that the conventionally annealed $Fe_{69.5}Co_3Nb_2Mo_{1.5}Si_{14}B_9Cu_1$ nanocrystalline alloy exhibits superior static soft magnetic properties: high μ_e (50,900 at 1 kHz) coupled with low H_c (0.54 A/m) [27]. This combination of characteristics is attractive and significant for high-frequency applications. However, its μ_e deteriorated rapidly during the medium-to-high frequency regime, dropping to a low value of 19,200 at 100 kHz, severely limiting its practical applicability. In this work, a stepwise transverse magnetic field annealing strategy is employed to address this bottleneck. A critical microstructural distinction is revealed of which the grain size remains invariant at ~12 nm, whilst the crystalline volume fraction (V_{cry} to ~70.6%) is significantly enhanced by stepwise strategy. The evolution of domain structure demonstrates that the controlled reduction of K_u fosters a highly uniform strip-shaped domain configuration, facilitating a transition from pinning-reduced domain wall displacement at low fields to a rotation-assisted process accompanied by domain splitting at intermediate fields. By precisely tailoring K_u and refining the domain structure, high and stable permeability ($\mu_e \approx 46{,}000$ at 1 kHz and 29,300 at 100 kHz) is achieved alongside reduced P_{cv} and H_c, demonstrating the alloy's strong potential for high-frequency WBG-based power-electronic applications.

2. Experimental procedure

Alloy ingot with compositions of $Fe_{69.5}Co_3Nb_2Mo_{1.5}Si_{14}B_9Cu_1$ was prepared by induction melting the mixtures of Fe, Co, Nb, Mo, Si, B and Cu with 99.99 wt% under an argon atmosphere. The as-spun ribbon was fabricated using a single-roller melt spinning process, with a thickness of 20 ± 2 μm. The annealing of the samples was carried out using a vacuum rotating magnetic field heat treatment furnace (NMS-CCRCLI, Chengdu Zhongke New Materials Technology and Engineering Co., Ltd). For all annealing treatments, a constant heating rate of 10 K/min was maintained to achieve the target temperatures. The thermal profile was regulated by a high-precision Proportional-Integral-Derivative (PID) controller. Ribbon segments with a length of 4–5 cm were sealed in quartz tubes and subjected to three annealing routes as depicted in Fig. 1**(a)**. Fig. S1 demonstrates that 818 K is the optimal annealing temperature for achieving enhanced soft magnetic properties. Normal annealing (NA) processed at 818 K for 30 min without a magnetic field ($H = 0$ Oe). Single-step transverse magnetic-field annealing (TFA1) processed at 818 K for 30 min under a magnetic field of 1000 Oe, and stepwise transverse magnetic-field annealing (NA+TFA2) processed at 818 K for 30 min ($H = 0$ Oe) followed by a second stage at 573 K for 120 min under a 1000 Oe field. Fig. 1**(b)** displays the prepared ribbon specimens and corresponding annular samples, and Fig. 1**(c)** illustrates the application module of Fe-based nanocrystalline alloys in new energy vehicles.

Thermal properties were analyzed by a differential scanning calorimeter (DSC, Netzsch 404 F3). Initial magnetization curves and hysteresis loops were measured using a vibrating sample magnetometer (VSM, Lake Shore 7407), and B_s was determined under an applied field of 800 kA/m. μ_e, H_c, and P_{cv} were measured by impedance analyzer (Keysight, E4990A), DC B-H loop tracer (Riken BHS-40) under a maximum field of 1 kA/m, and AC *B-H* loop tracer (Riken AC BH-100), respectively. The microstructure was characterized using X-ray diffraction (XRD, Bruker D8-Discover) with Cu-K_α radiation, and high-resolution transmission electron microscopy (HRTEM, Talos F200X) equipped with energy-dispersive X-ray spectroscopy (EDS). The average grain size (D_{av}) of the precipitated α-Fe(Co) phase was determined via TEM by analyzing at least five independent regions for each sample state. The number density of the nanocrystals (N_d) was calculated using the formula $N_d = N/\ (A \times D_{av})$, where N denotes the number of nanocrystals within the area A of TEM image. The overall V_{cry} was estimated using the equation $V_{cry} = N_d \pi D_{av}^3/6$ [28]. The resulting values are reported as arithmetic means with experimental errors quantified by standard deviations and 95% confidence intervals. The magnetic domain was analyzed employing a magneto-optical Kerr microscope (Evico Magnetics GmbH, em-Kerr-highres).

3. Results and discussion

Fig. 2**(a)** exhibits a broad diffuse halo peak characteristic of an amorphous structure, confirming that the as-spun $Fe_{69.5}Co_3Nb_2Mo_{1.5}Si_{14}B_9Cu_1$ alloy is fully amorphous. The DSC curve in Fig. 2**(b)** reveals two exothermic peaks. The first corresponds to the precipitation of the α-Fe phase, while the second is associated with the precipitation of (Fe, Co)-B phase. The primary ($T_{x1} = 816$ K) and secondary ($T_{x2} = 918$ K) crystallization temperatures yield a large separation ($\Delta T = T_{x2}$ - $T_{x1} = 152$ K), providing a broad processing window that facilitates the controllable nucleation of the α-Fe (Co) phase while effectively suppressing the early formation of secondary phases. This controlled nanocrystallization behavior is a prerequisite for achieving optimal soft magnetic performance. Additionally, a subtle endothermic peak at 588 K marks the Curie temperature (T_C), reflecting the transition from long-range ferromagnetic order to the paramagnetic state. These thermal insights guided the precise selection of annealing temperatures for the subsequent heat treatments to promote the optimal development of the nanocrystalline phase.

Fig. 3 compares the magnetic properties of $Fe_{69.5}Co_3Nb_2Mo_{1.5}Si_{14}B_9Cu_1$ alloy after NA, TFA1 and NA+TFA2. The specific performance values are listed in Table 1. The frequency dependence of μ_e is plotted in Fig. 3**(a)**. While μ_e naturally decreases with frequency for all samples, the NA treated sample exhibits a relatively rapid decay, serving as a baseline with a μ_e of 19,200 at 100 kHz. In contrast, the application of a transverse field consistently enhances high-frequency performance by facilitating a more ordered domain configuration and easing magnetization rotation [29,30], with the stepwise NA + TFA2 strategy achieving

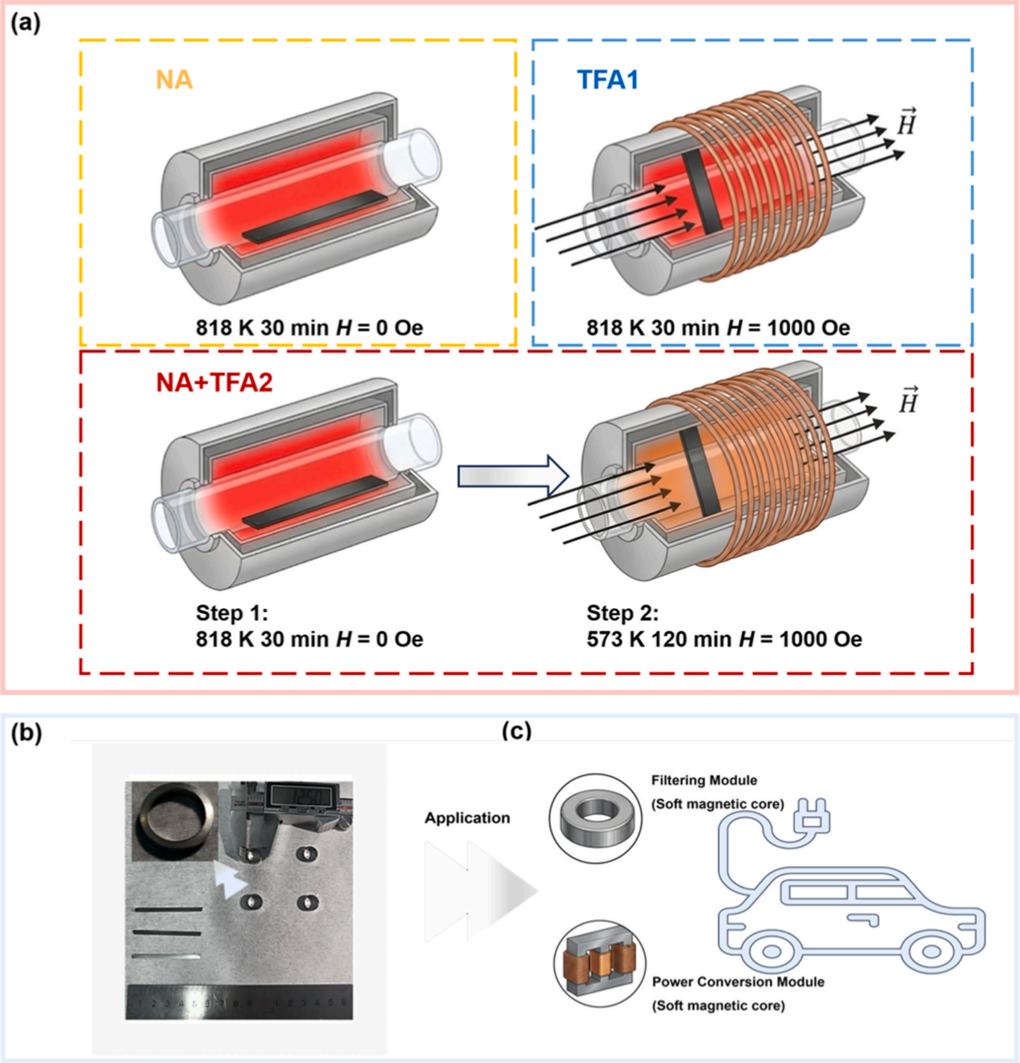

Fig. 1. (a) Optimal process parameters for different heat treatment processes, (b) alloy ribbons and corresponding annular samples, (c) application module of Fe-based nanocrystalline alloys in new energy vehicles.

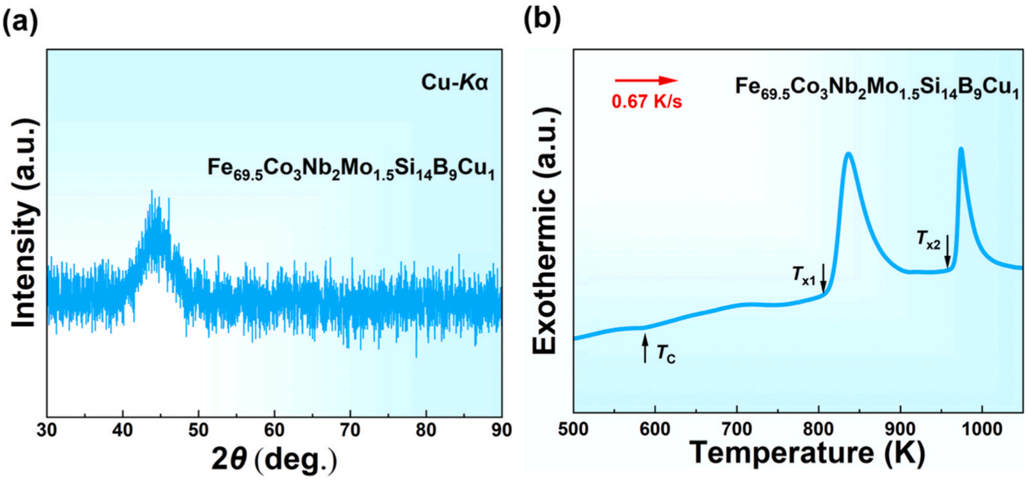

Fig. 2. Structural and thermal characterization of the as-spun $Fe_{69.5}Co_3Nb_2Mo_{1.5}Si_{14}B_9$ alloy. (a) XRD pattern, (b) DSC curve.

the highest stability across the entire 1–100 kHz range. Notably, at 100 kHz, μ_e rises significantly to 27,000 (TFA1) and peaks at 29,300 (NA + TFA2), corresponding to substantial improvements of ~40% and ~52% than NA, respectively. This underscores the superior effectiveness of the stepwise route in mitigating frequency-dependent deterioration. This exceptional performance validates the proposed mechanism; this is

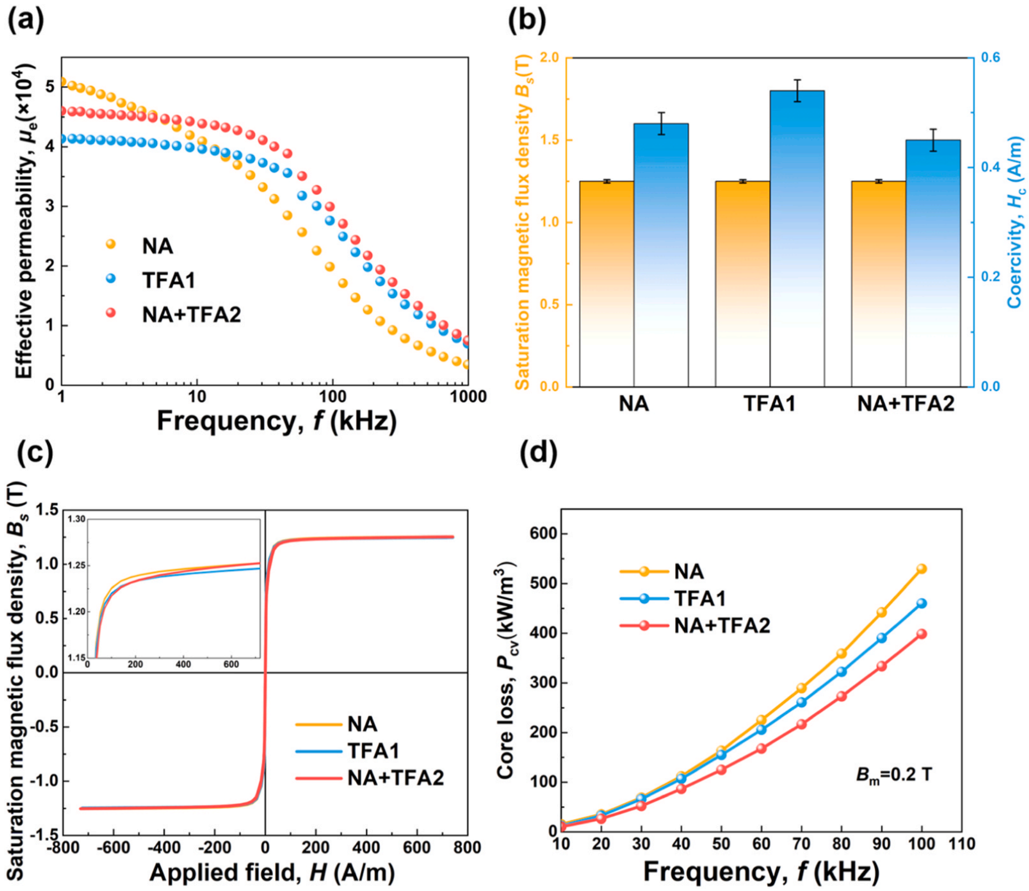

Fig. 3. Magnetic properties of $Fe_{69.5}Co_3Nb_2Mo_{1.5}Si_{14}B_9Cu_1$ alloy under NA, TFA1, NA+TFA2 treatment. (a) μ_e as a function of frequency, (b) H_c and B_s, (c) hysteresis loops with an inset showing the saturation region, (d) P_{cv} as a function of f at a maximum magnetic flux density (B_m) of 0.2 T.

Table 1
The soft magnetic properties of $Fe_{69.5}Co_3Nb_2Mo_{1.5}Si_{14}B_9Cu_1$ alloy at optimal annealing treatments for NA, TFA1 and NA+TFA2 samples.

Sample	μ_e			H_c	B_s	P_{cv}
	1 kHz	10 kHz	100 kHz	(A/m)	(T)	0.2 T/100 kHz (kW/m^3)
NA	50,900	41,300	19,200	0.49	1.25	530
TFA1	41,300	39,700	27,000	0.54	1.25	460
NA+TFA2	46,000	44,100	29,300	0.45	1.25	398

likely because the strategy can independently control the nanocrystalline structure and magnetic anisotropy. By applying the magnetic field only at a low temperature after crystallization, the process overcomes the anisotropy regulation limitations inherent to single-step annealing (TFA1), thereby realizing superior domain refinement and magnetic stability [30,31]. NA+TFA2 treated sample exhibits markedly the lowest H_c (0.49 A/m) compared to both the NA (0.54 A/m) and TFA1 counterparts (0.45 A/m). From the hysteresis loops, the specific annealing protocols have no effect on the B_s amongst samples with a consistent value of ~1.25 T. Fig. 3**(d)** displays the P_{cv} at $B_m = 0.2$ T with respect to frequency for the NA, TFA1, and NA+TFA2 treated samples. While P_{cv} naturally increases with increasing frequency across all samples, it decreases significantly following the specific stepwise annealing strategy. Specifically, at 100 kHz, the P_{cv} drops from 530 kW/m^3 for the NA sample and 460 kW/m^3 for the TFA1 sample to a minimum of 398 kW/m^3 for the NA+TFA2 sample.

To demonstrate the superior high-frequency response of the present alloy, Fig. 4**(a)** benchmarks its μ_e against representative Fe-based nanocrystalline systems reported in the literature [3,6,8,10,13,32–39]. It can be clearly seen that the μ_e at 100 kHz has been significantly improved in this work. While conventional alloys such as FeZrB and FeSiBPCuC show relatively limited permeability, the alloy developed herein achieves an unprecedented performance level. As highlighted by the arrow, the μ_e in this work represents a substantial increase of 17.2% compared to the best-performing counterpart (FeSiBNbCuP) currently available. This result indicates that the bottleneck for enhancing high-frequency permeability in Fe-based nanocrystalline alloys has been successfully broken. In addition to high permeability, minimizing energy dissipation is critical for application. Fig. 4**(b)** compares the P_{cv} measured at 100 kHz and $B_m = 0.2$ T. The plotted data reveals that the present alloy occupies a distinct region characterized by low P_{cv}, significantly outperforming other systems like FeZrB and FeZrBNb. This advantageous combination, simultaneously achieving record-breaking μ_e and suppressed P_{cv}, not only underscores the effectiveness of the NA + TFA2 strategy but also positions this alloy as an outstanding candidate for next-generation industrial applications, such as energy-efficient transformers and high-frequency motors.

Fig. 5 illustrates the microstructural evolution of the $Fe_{69.5}Co_3Nb_2Mo_{1.5}Si_{14}B_9Cu_1$ alloy following NA, TFA1, and NA+TFA2 treatments. All samples display sharp fundamental peaks indexed to the bcc α-Fe (Co) phase, confirming the complete crystallization of the amorphous precursor under each annealing condition (Fig. 5**(a)**). To quantify the microstructural parameters, the main (110) diffraction peak was analyzed using Voigt profile fitting (Fig. 5**(b)**), which allows for the deconvolution of grain-size broadening from lattice strain contributions [40]. As illustrated in Fig. 5**(c)**, this analysis reveals average grain sizes of 12.3 nm, 11.9 nm, and 12.2 nm for the NA, TFA1, and NA+TFA2 states, respectively. The extracted microstrain values, summarized in Fig. 5**(d)**, reveal a pronounced dependence on the annealing protocol.

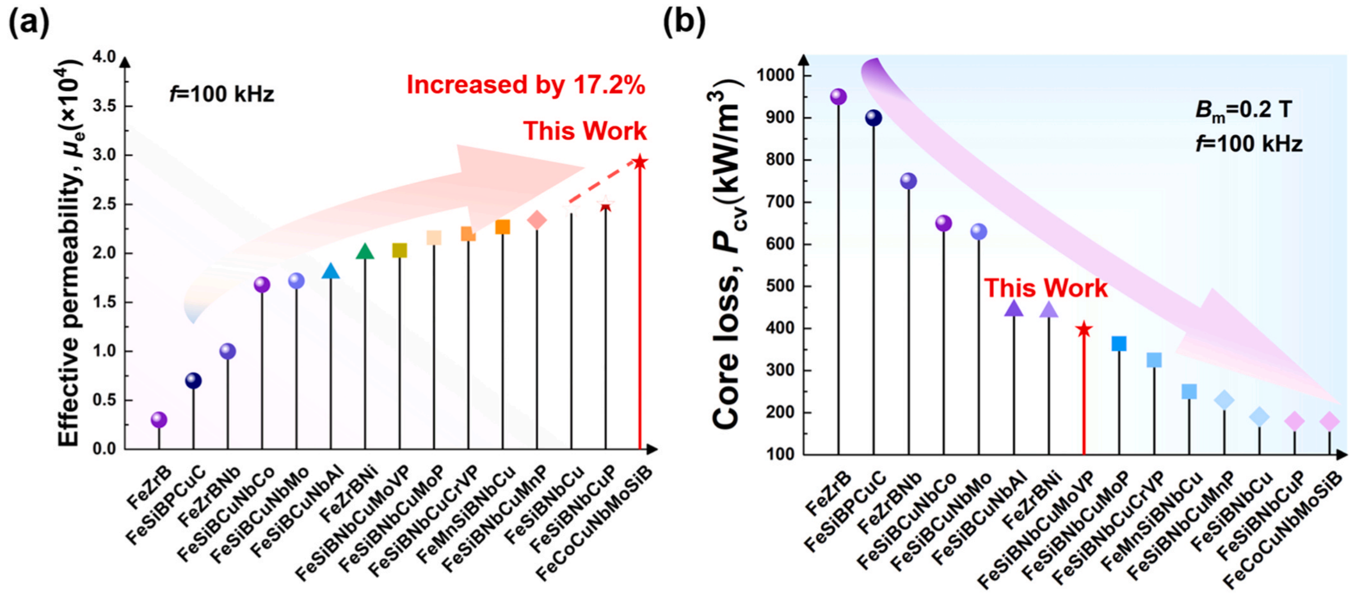

Fig. 4. Comparison of (a) μ_e and (b) P_{cv} among various Fe-based nanocrystalline alloys in the reported literature, measured at $B_m = 0.2$ T and $f = 100$ kHz [3,6,8,10,13,32–39].

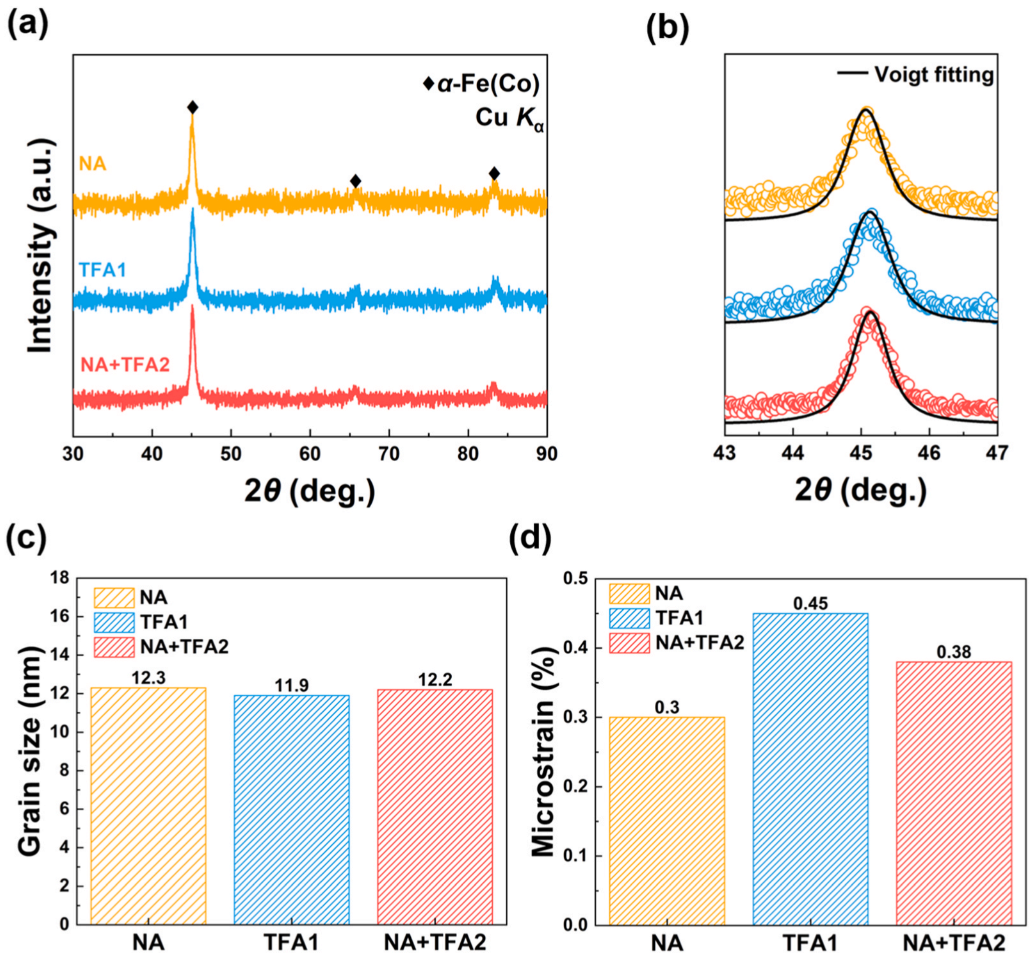

Fig. 5. Structural analysis of $Fe_{69.5}Co_3Nb_2Mo_{1.5}Si_{14}B_9Cu_1$ alloy under different treatment conditions. (a) XRD patterns for NA, TFA1, and NA+TFA2 samples, (b) Voigt fitting of the main diffraction peak, (c) grain size and (d) microstrain calculated from XRD broadening.

The NA sample exhibits the lowest microstrain (~0.30%), consistent with a well-relaxed nanocrystalline structure formed during conventional annealing. In contrast, the TFA1 treatment induces a significant increase in microstrain to ~0.45%, suggesting enhanced lattice distortion or interfacial stress introduced when crystallization occurs under an applied transverse magnetic field. Notably, the NA+TFA2 strategy yields an intermediate microstrain level of ~0.38%. This indicates that by independent control of nanocrystalline structure and magnetic anisotropy the excessive stress accumulation inherent to the TFA1 process is effectively mitigated. These distinctions in microstrain are critical, as local strain fields strongly influence magneto-elastic coupling and domain-wall dynamics, thereby governing the macroscopic soft magnetic performance [41].

To elucidate the structural origins of the superior soft magnetic performance observed in the NA+TFA2 sample, a detailed microstructural analysis was conducted using TEM. Fig. 6 presents the bright-field images and corresponding SAED patterns for the annealed alloys. As visualized in Fig. 6**(a, d, g)**, all samples exhibit a uniform nanocrystalline architecture consisting of ultrafine equiaxed α-Fe(Co) grains embedded within a residual amorphous matrix. The sharp diffraction rings in the SAED patterns (Fig. 6**(b, e, h)**) confirm the random orientation of these bcc crystallites. Quantitative analysis of the grain size distributions reveals a critical insight: while the grain size is invariant, the crystalline density evolves significantly. As shown in the Log-Normal fitting (Fig. 6**(c, f, i)**), the D_{av} remains constant at ~12 nm across all treatments. This finding is consistent with the crystallite sizes

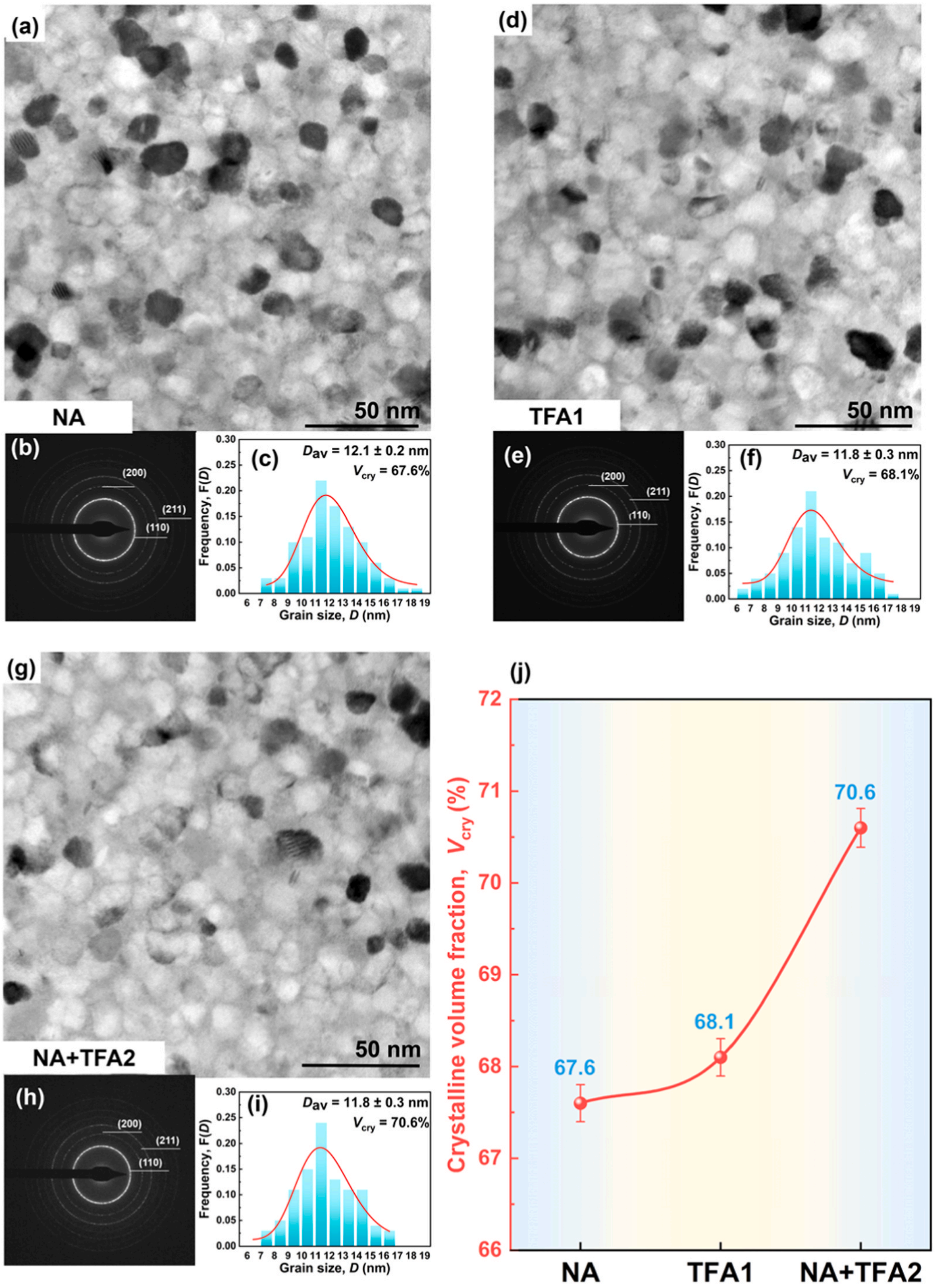

Fig. 6. Bright-field TEM images, SAED patterns, grain size distribution of $Fe_{69.5}Co_3Nb_2Mo_{1.5}Si_{14}B_9Cu_1$ nanocrystalline alloys subjected to (a)-(c) NA, (d)-(f) TFA1, and (g)-(i) NA+TFA2 treatment, (j) variations of $V_{cry,}$ with error bars representing the 95% confidence intervals.

obtained from the XRD Voigt fitting presented in Fig. 5**(c)**, which validates the reliability of the microstructural analysis. However, a distinct upward trend is observed in the V_{cry}, which rises from 67.6% (NA) and 68.1% (TFA1) to a peak of 70.6% for the NA+TFA2 sample. This elevated V_{cry} plays a pivotal role in optimizing magnetic softness. A higher fraction of ferromagnetic nanocrystals reduces the intergranular spacing, thereby strengthening the ferromagnetic exchange coupling between adjacent grains. Since the grain size is well below the ferromagnetic exchange length, this enhanced coupling effectively averages out the magnetocrystalline anisotropy. Consequently, the coexistence of this high crystalline volume fraction with the tailored uniaxial anisotropy induced by the stepwise field annealing synergistically minimizes H_c and maximizes μ_e, as evidenced in Fig. 3. The consistent grain size across samples suggests that the variations in soft magnetic properties do not originate from geometrical confinement. Instead, the performance enhancement is driven by the precise regulation of induced anisotropy, underpinned by the evolution of the crystalline volume fraction. Although the increase in V_{cry} is subtle, it is sufficient to enhance the intergranular exchange coupling, thereby facilitating the efficient averaging of magnetocrystalline anisotropy in the NA+TFA2 sample [20,42].

To visually elucidate the elemental distribution and phase stability, mapping was performed as Fig. 7. The maps reveal a consistent elemental partitioning behavior across the NA, TFA1, and NA+TFA2 samples, indicating that the magnetic field treatments do not disrupt the fundamental chemical order. The distribution follows a clear core-shell-like logic: Fe and Co are homogeneously enriched within the nanocrystalline grains, while Cu appears as distinct, dispersed clusters. This clustering is driven by the large positive mixing enthalpy between Fe and Cu (+13 kJ/mol), enabling Cu to serve as heterogeneous nucleation sites for the α-Fe (Co) phase. Crucially, Nb and Mo are rejected from the crystalline lattice, forming a reticular enrichment in the intergranular amorphous matrix. This explains the invariant grain size (~12 nm) observed in Fig. 6. The role of the magnetic field can be further understood through classical nucleation theory. Applying a magnetic field below T_C introduces a magnetic volume free energy (ΔG_V^{mag}), thereby reducing the free energy barrier (ΔG^*) for nucleation [43]. During the TFA1 process, 818 K is above the T_C of the amorphous precursor, which renders the magnetic driving force ineffective and the high temperature triggers a competition between nucleation and grain growth. Conversely, magnetic annealing at 573 K in the NA+TFA2 process can maximize the ΔG_V^{mag} and drive the abundant formation of ultrafine secondary nuclei. This theoretical mechanism aligns perfectly with our experimental observation: the magnetic field promotes the formation of more nuclei (increasing the crystalline volume fraction to 70.6%) [44], while the diffusion-slow Nb/Mo barrier strictly limits their growth, resulting in a high-density, ultrastable microstructure [11,35].

The field-driven evolution of magnetic domains in NA, TFA1 and NA+TFA2 samples are illustrated in Fig. 8. The NA sample displays curved and irregular domain walls at zero field, reflecting the dominance of random magnetic anisotropy. Numerous pinning sites impede domain-wall motion, and magnetization occurs primarily through domain-wall displacement. As the static field increases, the walls progressively straighten and shift, reaching full alignment at ~0.48 kA/m, consistent with its low-frequency permeability. In the TFA1 sample, the transverse magnetic field introduces a pronounced uniaxial anisotropy, resulting in broader, more regularly spaced stripe domains. Even at low fields (0.16 kA/m), localized magnetization rotation is visible, accompanied by modest wall displacement. The coexistence of domain-wall motion and non-uniform rotation indicates a hybrid magnetization mechanism derived from field-induced anisotropy and residual microstrain [22]. The NA + TFA2 sample shows the most uniform strip-shaped configuration. With increasing field, domain walls shift smoothly and widen, indicating reduced pinning and lower energy barriers for domain motion. This sample reaches saturation at a lower static field compared with TFA1, consistent with its higher μ_e at high frequency (1 kHz). At intermediate fields (~0.32 kA/m), domain splitting and non-uniform rotation begin to emerge, marking a transition from wall-dominated to rotation-assisted magnetization. This behavior aligns with literature showing that materials with reduced magnetic anisotropy minimize total magnetic energy through domain nucleation and splitting, leading to improved high-frequency performance [45]. Together, the domain observations demonstrate that the NA + TFA2 treatment achieves an optimal balance of anisotropy: low enough to facilitate efficient domain-wall motion at low frequencies, yet sufficiently uniform to promote stable rotation mechanisms at higher frequencies. This synergy explains its superior permeability and reduced P_{cv} across the medium–high frequency range.

Demagnetization-corrected initial magnetization curves were measured for the NA, TFA1 and NA + TFA2 samples with the field applied transverse to the ribbon axis. The correction was carried out using the reciprocal susceptibility method [42], in which the lower limit value of $1/\chi^*$ was evaluated to determine the demagnetization factor (N_D). Based on this analysis, N_D was found to be 9×10^{-3} [46]. The effective magnetic field (H_{eff}) was then calculated using:

$$H_{eff} = H_{app} - N_D M \tag{1}$$

The induced anisotropic property K_u can be calculated according to

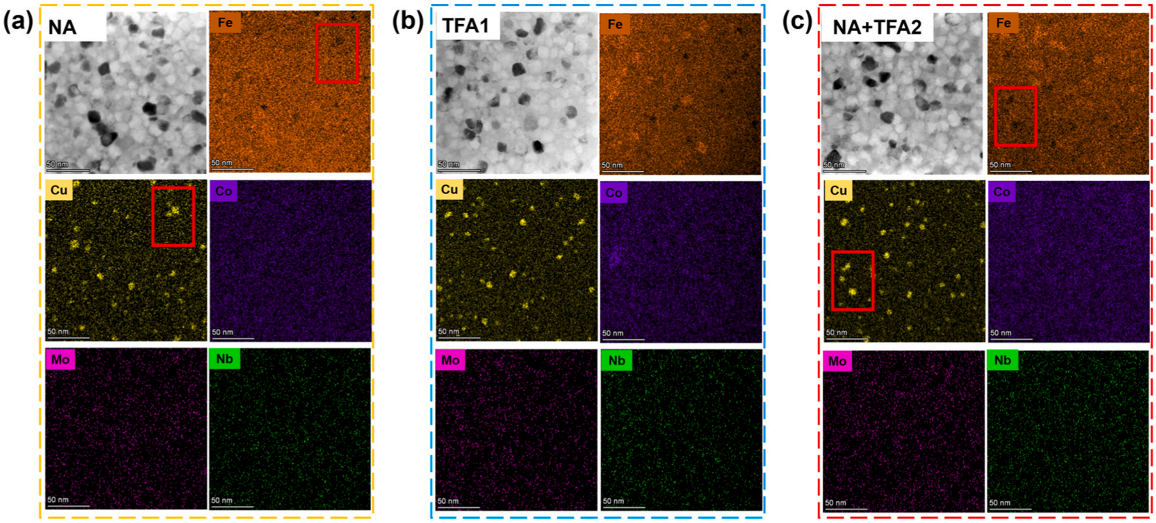

Fig. 7. Element mapping of $Fe_{69.5}Co_3Nb_2Mo_{1.5}Si_{14}B_9Cu_1$ nanocrystalline alloys subjected to (a) NA, (b) TFA1 and (c) NA+TFA2 treatment.

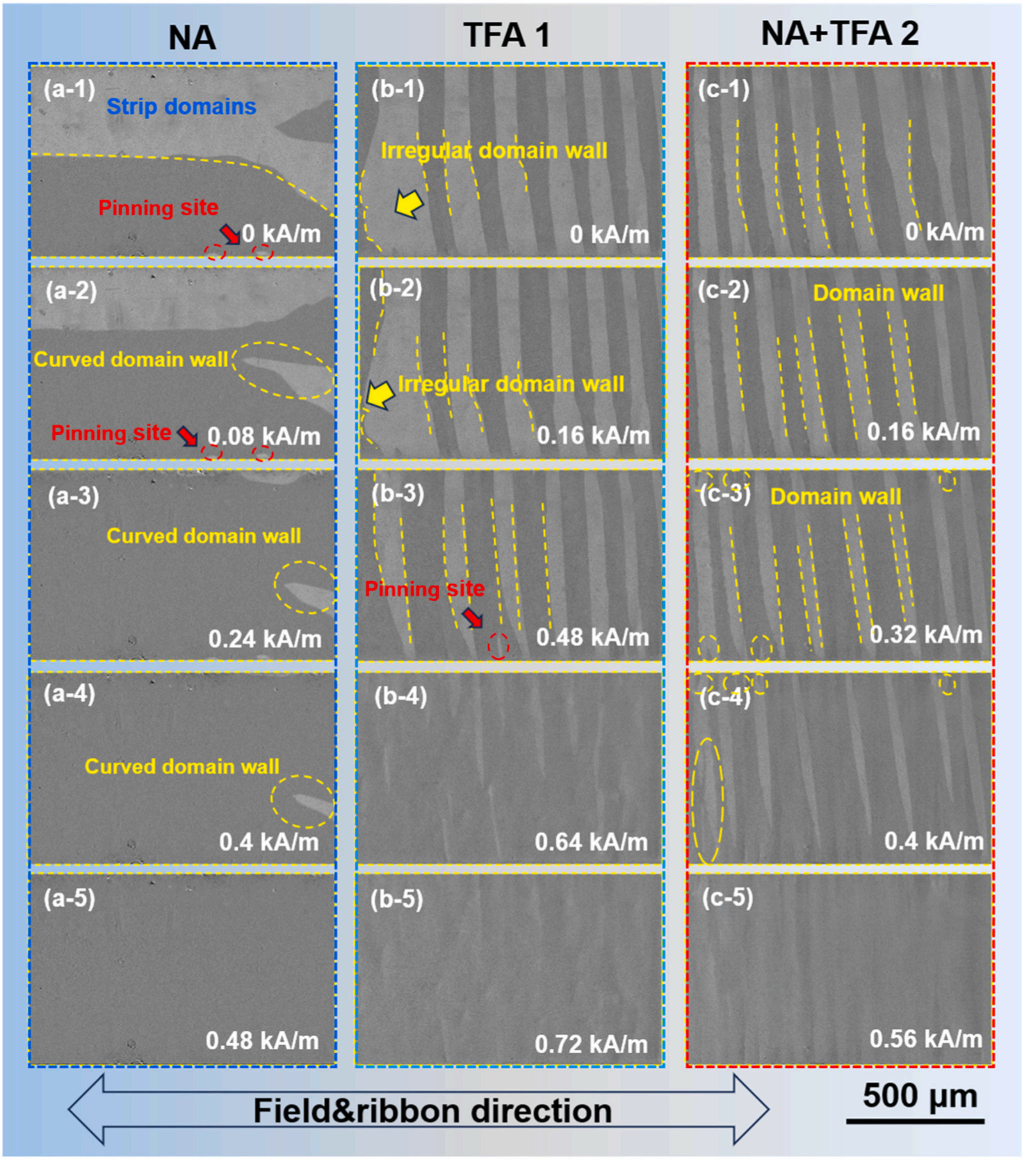

Fig. 8. Magnetic domain evolution of $Fe_{69.5}Co_3Nb_2Mo_{1.5}Si_{14}B_9Cu_1$ alloys under dynamic magnetic fields following optimal annealing treatments: (a) NA, (b) TFA1 and (c) NA+TFA2.

the following formula:

$$K_u = \frac{H_k B_s}{2} \tag{2}$$

To visually elucidate the impact of anisotropy on magnetic softness, the K_u and anisotropy field (H_k) were quantified in Fig. 9. A clear hierarchy is observed: TFA1 ($K_u \approx 28$ J/m^3) > NA (25 J/m^3) > NA+TFA2 (19.4 J/m^3). The origin of these variations lies in the competition between atomic ordering and stress relaxation. For the TFA1 sample, the high K_u originates from the strong directional ordering of Fe-Co atom pairs along the field direction. The NA sample retains a moderate effective anisotropy due to residual random stresses despite the absence of an external field. The NA+TFA2 strategy uniquely enables the independent control of these factors: the low-temperature field annealing relaxes the internal stresses inherent to the NA state without inducing the excessive atomic locking seen in TFA1. This minimization of K_u is the direct structural origin of the record-breaking permeability. According to the coherent rotation model for transverse-field annealed alloys, μ_e is inversely proportional to the induced anisotropy [30]:

$$\mu_e = \frac{J_s^2}{2\mu_0 K_\mu} \tag{3}$$

The distinct reduction of K_u in the NA+TFA2 sample significantly lowers the energy barrier for magnetization rotation. This allows the magnetic moments to respond more sensitively to weak external fields, thereby explaining why this alloy achieves the highest μ_e (≈ 29,300 at 100 kHz) value and stability spanning wide medium-high frequency.

4. Conclusions

In this study, the high-frequency magnetic behavior of $Fe_{69.5}Co_3Nb_2Mo_{1.5}Si_{14}B_9Cu_1$ nanocrystalline alloys was systematically tailored through a stepwise transverse magnetic field annealing (NA + TFA2) strategy. By independently regulating the crystallization process and anisotropy induction, our findings demonstrate that the superior magnetic softness is not driven by grain size reduction, which remains invariant at ~12 nm across all treatments, but largely by the precise engineering of lattice strain and phase fraction. Specifically, the NA + TFA2 strategy mitigates the lattice microstrain of 0.38% inherent to

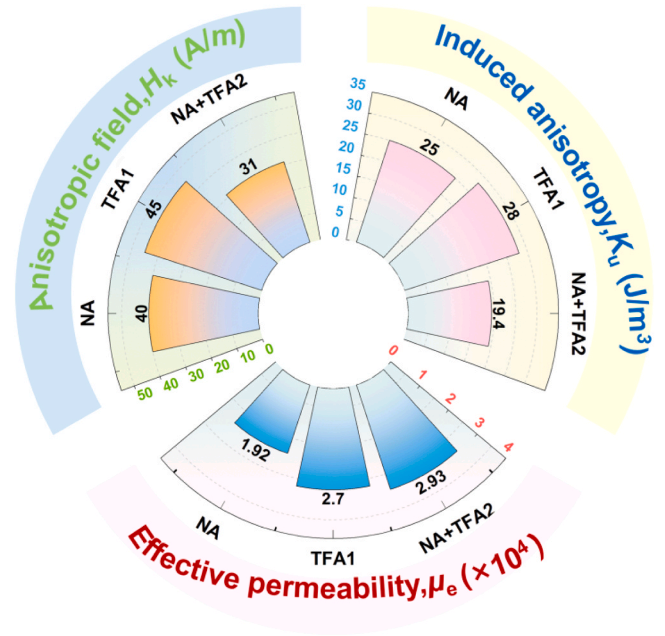

Fig. 9. Comparison of the H_k, K_u and μ_e for the optimally annealed $Fe_{69.5}Co_3Nb_2Mo_{1.5}Si_{14}B_9Cu_1$ alloy in NA, TFA1 and NA+TFA2 states.

direct field annealing while simultaneously maximizing the crystalline volume fraction of 70.6%, resulting in a minimized K_u of 19.4 J/m^3 . The optimized alloy exhibits an exceptional combination of frequency-stable μ_e of 29,300 at 100 kHz, ultra-low H_c of 0.45 A/m, and significantly suppressed P_{cv} of 398 kW/m^3 at 100 kHz, 0.2 T. These results confirm that optimizing the interplay between lattice relaxation and induced anisotropy is key to breaking the permeability-loss trade-off, providing a scalable pathway for developing next-generation low-loss alloys for energy-efficient high-frequency applications.

CRediT authorship contribution statement

Jifeng Zhou: Writing – original draft, Formal analysis, Investigation. **Chi Ren**: Data curation, Formal analysis, Investigation. **Qianqian Liu**: Data curation, Methodology, Investigation. **Jun Li**: Formal analysis. **Fan Hu:** Investigation. **Qianqian Wang**: Investigation. **Xingdu Fan**: Methodology. **Zhe Jia**: Investigation. **Qiang Luo**: Formal analysis, Supervision. **Zhijun Guo**: Funding acquisition, Methodology, Supervision, Conceptualization, Writing – review & editing. **Baolong Shen**: Funding acquisition, Project administration, Supervision.

Declaration of Competing Interest

The authors declare that they have no known competing financial interests or personal relationships that could have appeared to influence the work reported in this paper.

Acknowledgements

This work was financially supported by the National Key R&D Program of China (No. 2022YFB3804100), the National Natural Science Foundation of China (No. 52231005), the Science Technology Development Program of Yixing (No. C2024002). The authors thank the Center for Fundamental and Interdisciplinary Sciences of Southeast University for the support in magnetic domain measurement.

Appendix A. Supporting information

Supplementary data associated with this article can be found in the online version at doi:10.1016/j.jallcom.2026.188535.

Data availability

Data will be made available on request.

References

[1] J.M. Silveyra, E. Ferrara, D.L. Huber, et al., Soft magnetic materials for a sustainable and electrified world[J], Science 362 (6413) (2018) eaao0195.
[2] M. Niethammer, M. Widmann, T. Rendler, et al., Coherent electrical readout of defect spins in silicon carbide by photo-ionization at ambient conditions[J], Nat. Commun. 10 (1) (2019) 5569.
[3] O. Gutfleisch, M.A. Willard, E. Brück, et al., Magnetic materials and devices for the 21st century: stronger, lighter, and more energy efficient[J], Adv. Mater. 23 (7) (2011) 821–842.
[4] W. Liu, H. Zhang, J.-A. Shi, et al., A room-temperature magnetic semiconductor from a ferromagnetic metallic glass[J], Nat. Commun. 7 (1) (2016) 13497.
[5] X. Li, L. Lou, W. Song, et al., Novel bimorphological anisotropic bulk nanocomposite materials with high energy products[J], Adv. Mater. 29 (16) (2017) 1606430.
[6] Z.H. Stachurski, G. Wang, An introduction to metallic glasses and amorphous metals, Elsevier, Netherlands, 2021.
[7] M. Nakamura, O. Ishii, S. Horikoshi, et al., Application of Fe-based nanocrystalline ribbon to a noise filter and a shielded cable[J], IEEE Trans. Magn. 40 (4) (2004) 2733–2735.
[8] Y. Yoshizawa, S. Oguma, K. Yamauchi, New Fe-based soft magnetic alloys composed of ultrafine grain structure[J], J. Appl. Phys. 64 (10) (1988) 6044–6046.
[9] H. Xiao, Y. Dong, A. He, et al., Magnetic softness and magnetization dynamics of FeSiBNbCu(P, Mo) nanocrystalline alloys with good high-frequency characterization[J], J. Magn. Magn. Mater. 478 (2019) 192–197.
[10] H. Li, A. Wang, T. Liu, et al., Design of Fe-based nanocrystalline alloys with superior magnetization and manufacturability[J], Mater. Today 42 (2021) 49–56.
[11] Y. Fan, C. Jin, M. Wang, et al., Nb microalloying enhances the amorphous forming ability and soft magnetic properties of high B_s Fe-based nanocrystalline alloys[J], J. Alloy. Compd. 1044 (2025) 184627.
[12] M. Jiang, M. Cai, J. Zhou, et al., Superior high-frequency performances of Fe-based soft-magnetic nanocrystalline alloys[J], Mater. Today Nano 22 (2023) 100307.
[13] J. Yao, C. Zhao, S. Lv, et al., Structural relaxation and magnetic properties of multicomponent Fe-based amorphous alloy ribbons, Rare Met. 44 (2025) 10621–10631.
[14] Y. Meng, S. Pang, C. Chang, et al., Effects of Si on the microstructure, soft magnetic properties and bendability of rapidly-annealed nanocrystalline Fe–Si–B–P–Cu alloy ribbons[J], J. Alloy. Compd. 940 (2023) 168799.
[15] C. Liu, A. Inoue, F.L. Kong, et al., Fe-B-Si-C-Cu amorphous and nanocrystalline alloys with ultrahigh hardness and enhanced soft magnetic properties[J], J. Non-Cryst. Solids 554 (2021) 120606.
[16] A.I. Bazlov, D.A. Milkova, E.N. Zanaeva, et al., Formation, thermal stability and soft magnetic properties of Fe-Co-B-Si amorphous alloys with ultrahigh saturation magnetic induction of 2.0 T[J], J. Alloy. Compd. 1006 (2024) 176247.
[17] B. Shen, A. Inoue, Fabrication of large-size Fe-based glassy cores with good soft magnetic properties by spark plasma sintering[J], J. Mater. Res. 18 (9) (2003) 2115–2121.
[18] Z.J. Guo, J. Li, J.H. Fu, et al., Continuous stress annealing enables ultralow-loss Fe-based amorphous alloys with superior magnetic softness for industrial manufacturing[J], Rare Met. 45 (3) (2026) e70252.
[19] M. Cai, Z. Guo, L. Li, et al., Obtaining extremely low coercivity of high B_s FeCoBSiCPCu nanocrystalline alloys through modulation of magnetic anisotropy [J], J. Mater. Sci. & Technol. 207 (2025) 105–112.
[20] L. Wang, K. Wang, Q. Chen, et al., Tuned exchange coupling and anisotropy via magnetic field-assisted annealing for high-performance nanocrystalline soft magnetic alloys[J], Acta Mater. 292 (2025) 121030.
[21] R. Madugundo, O. Geoffroy, T. Waeckerle, et al., Improved soft magnetic properties in nanocrystalline FeCuNbSiB Nanophy® cores by intense magnetic field annealing[J], J. Magn. Magn. Mater. 422 (2017) 475–478.
[22] Herzer G. Amorphous, and Nanocrystalline Soft Magnets, in: G.C. Hadjipanayis (Ed.), Magnetic Hysteresis in Novel Magnetic Materials, Dordrecht, Springer, Netherlands, 1997, pp. 711–730.
[23] G. Herzer, Magnetic field induced anisotropy in nanocrystalline Fe-Cu-Nb-Si-B alloys[J], Materials Science Engineering A 181-182 (1994) 876–879.
[24] S. Flohrer, R. Schäfer, C. Polak, et al., Interplay of uniform and random anisotropy in nanocrystalline soft magnetic alloys[J], Acta Mater. 53 (10) (2005) 2937–2942.
[25] S. Flohrer, R. Schäfer, J. McCord, et al., Dynamic magnetization process of nanocrystalline tape wound cores with transverse field-induced anisotropy[J], Acta Mater. 54 (18) (2006) 4693–4698.
[26] S. Flohrer, R. Schäfer, J. McCord, et al., Magnetization loss and domain refinement in nanocrystalline tape wound cores[J], Acta Mater. 54 (12) (2006) 3253–3259.
[27] Z. Guo, J. Zhou, Q. Liu, et al., Stress-induced anisotropy for MHz-stable permeability in Fe-based nanocrystalline alloys[J], Sci. China Mater. 69 (2026) 1518–1528.
[28] X. Jia, Y. Dong, L. Zhang, et al., Influence of static magnetic field on rapid solidified structure and nanocrystallization behavior of Fe–Si–B–Cu soft magnetic alloys with pre-existing α-Fe nanocrystals[J], J. Mater. Res. Technol. 24 (2023) 9594–9600.

[29] G. Herzer, Soft magnetic nanocrystalline materials[J], Scr. Metall. Et. Mater. 33 (10) (1995) 1741–1756.

[30] G. Herzer, Modern soft magnets: amorphous and nanocrystalline materials[J], Acta Mater. 61 (3) (2013) 718–734.

[31] G. Herzer, Nanocrystalline soft magnetic alloys[J], Handb. Magn. Mater. 10 (1997) 415–462.

[32] K. Suzuki, A. Makino, A. Inoue, et al., Low core losses of nanocrystalline Fe–M–B (M=Zr, Hf, or Nb) alloys[J], J. Appl. Phys. 74 (5) (1993) 3316–3322.

[33] Y. Yoshizawa, S. Fujii, D.H. Ping, et al., Magnetic properties of nanocrystalline FeMCuNbSiB alloys (M: Co, Ni)[J], Scr. Mater. 48 (7) (2003) 863–868.

[34] W. Lu, J. Fan, Y. Wang, et al., Microstructure and magnetic properties of $Fe_{72.5}Cu_1M_2V_2Si_{13.5}B_9$ (M=Nb, Mo, (NbMo), (MoW)) nanocrystalline alloys[J], J. Magn. Magn. Mater. 322 (19) (2010) 2935–2937.

[35] M. Xiao, Z. Zheng, L. Ji, et al., The role of V and Mo on crystallization process and magnetic properties of FeSiBCuNb alloys using in wide frequency scale[J], J. Non-Cryst. Solids 521 (2019) 119546.

[36] J. Zhou, X. Li, X. Hou, et al., Ultrahigh permeability at high frequencies via a magnetic-heterogeneous nanocrystallization mechanism in an iron-based amorphous alloy[J], Adv. Mater. 35 (40) (2023) 2304490.

[37] S. Guo, Y. Li, Y. Zhang, et al., Reduction of high-frequency core loss of a $Fe_{77.2}Si_{11}B_{8.5}Cu_{0.8}Nb_{2.5}$ soft magnetic nanocrystalline alloy by minor alloying[J], Acta Metall. Sin. (Engl. Lett.) 37 (11) (2024) 1984–1992.

[38] Y. Sun, J. Li, A. He, et al., Influence of microstructure and anisotropy on the high-frequency soft magnetic properties of nanocrystalline FeSiBNbCuP alloys[J], J. Magn. Magn. Mater. 560 (2022) 169639.

[39] F. Yang, B. Zhang, S. Man, et al., Enhanced thermal-operating stability of high-frequency magnetic behavior for FeMnSiBNbCu nano-structural cores via field-annealing[J], Vacuum 188 (2021) 110214.

[40] D. Balzar, Voigt-function model in diffraction line-broadening analysis[J], Defect Microstruct. Anal. Diffr. (1999) 94–126.

[41] M. Ohnuma, T. Yanai, K. Hono, et al., Stress-induced magnetic and structural anisotropy of nanocrystalline Fe-based alloys[J], J. Appl. Phys. 108 (2010) 093927.

[42] Y. Yoshizawa, K. Yamauchi, Effects of magnetic field annealing on magnetic properties in ultrafine crystalline Fe-Cu-Nb-Si-B alloys[J], IEEE Trans. Magn. 25 (5) (1989) 3324–3326.

[43] D. Holland-Moritz, F. Spaepen, The magnetic contribution to the driving force for crystal nucleation in undercooled Co–Pd melts[J], Philos. Mag. 84 (10) (2004) 957–966.

[44] R. Gautam, S. Hiramoto, N. Kulesh, et al., Ultra-low core loss in Fe-enriched soft magnetic ribbons enabled by nanostructure and high-frequency domain engineering[J], Nat. Commun. 16 (1) (2025) 8022.

[45] A.J. Schellekens, A. van den Brink, J.H. Franken, et al., Electric-field control of domain wall motion in perpendicularly magnetized materials[J], Nat. Commun. 3 (2012) 847.

[46] J.S. Blázquez, J. Marcin, F. Andrejka, et al., Anisotropy field distribution in soft magnetic Hitperm alloys submitted to different field annealing processes[J], J. Alloy. Compd. 658 (2016) 367–371.